Subtractive and Divisive Inhibition: Effect of Voltage-Dependent Inhibitory Conductances and Noise

Brent Doiron
André Longtin
Physics Department, University of Ottawa, Ottawa, Canada K1N 6N5

Neil Berman
Leonard Maler
Department of Cellular and Molecular Medicine, University of Ottawa, Ottawa, Canada K1H 8M5

The influence of voltage-dependent inhibitory conductances on firing rate versus input current (f-I) curves is studied using simulations from a new compartmental model of a pyramidal cell of the weakly electric fish *Apteronotus leptorhynchus*. The voltage dependence of shunting-type inhibition enhances the subtractive effect of inhibition on f-I curves previously demonstrated in Holt and Koch (1997) for the voltage-independent case. This increased effectiveness is explained using the behavior of the average subthreshold voltage with input current and, in particular, the nonlinearity of Ohm's law in the subthreshold regime. Our simulations also reveal, for both voltage-dependent and -independent inhibitory conductances, a divisive inhibition regime at low frequencies ($f < 40$ Hz). This regime, dependent on stochastic inhibitory synaptic input and a coupling of inhibitory strength and variance, gives way to subtractive inhibition at higher-output frequencies ($f > 40$ Hz). A simple leaky integrate-and-fire type model that incorporates the voltage dependence supports the results from our full ionic simulations.

1 Introduction

A current problem in single neuron computation is the characterization of the relation between the synaptic input current, I, received by a neuron and the frequency, f, of action potentials that the neuron generates in response to this input. Knowledge of this f-I relationship provides a simplified plausible description of neural input-output operations, which can be used to model networks of neurons (see, e.g., Abbott, 1991). Adaptive signal processing strategies have received much recent interest in the context of these f-I relationships (see, e.g., Nelson, 1994; Carandini & Hegger, 1994; Nelson & Paulin, 1995; Holt & Koch, 1997; Abbott, Varela, Sen, & Nelson, 1997; Tsodyks & Markram, 1997). One such strategy involves gain control via

feedforward and feedback inhibition. Such feedback alters the sensitivity of the neuron to excitatory input and thus modifies the f-I relationship.

Inhibitory transmission in the central nervous system is mediated primarily by $GABA_A$ and $GABA_B$ gated receptors. $GABA_B$ receptors are linked to potassium channels, and their activation results in long-lasting, large inhibitory postsynaptic potentials (IPSPs) with a relatively small conductance change. This inhibition has been referred to as "subtractive" since its primary effect has been hypothesized to reduce the effect of excitatory input linearly. The f-I curve is thus shifted to higher excitatory currents, but its shape is maintained. However, $GABA_A$ receptors are connected to chloride channels that have a reversal potential close to the resting membrane potential of the cell. When activated, these channels produce brief, relatively small, potential shifts, yet cause large conductance increases; this has been described as shunting inhibition. It was commonly thought that shunting gain control is divisive in nature; that is, the slope of the f-I curve is reduced under shunting (Rose, 1977; Koch & Poggio, 1992). However, Holt and Koch (1997) have demonstrated that in the suprathreshold regime, the effect of shunting synapses is subtractive.

Theoretical studies of such effects have assumed voltage-independent inhibitory conductances. However, there is substantial evidence that this is not the case. Segal and Barker (1984) and Yoon (1994) have obtained an increase in $GABA_A$ chloride conductance with depolarization in studies on rat hippocampal cells. Similar results have been obtained for glycine and $GABA_A$-activated chloride channels in fish brain (Faber & Korn, 1987; Legendre & Korn, 1995; Berman & Maler, 1998a). The putative mechanisms are thought to involve a voltage-dependent increase in channel open time (Segal & Barker, 1984; Faber & Korn, 1987; Legendre & Korn, 1995) and decrease in channel desensitization (see Yoon, 1994, and additional references therein).

We therefore reexamined the role of voltage-dependent inhibition in the sub- and suprathreshold regimes in determining the subtractive or divisive character of the inhibition. We inserted voltage dependence of shunting inhibition (chloride channels) into two neural models: (1) a new detailed compartmental model of the basilar pyramidal cell of the electrosensory lateral line lobe (ELL) of the weakly electric fish *Apteronotus letorhynchus* and (2) a simple leaky integrate-and-fire model (LIF). We developed the first model because of the detailed electrophysiological knowledge of inhibition in the ELL (Berman & Maler, 1998a, 1998b, 1998c). The second model was investigated for comparison with the first. Apart from its analytic tractability, it ensured that our results were not model dependent. Our findings can be summarized as follows:

- In the subthreshold regime, shunting inhibition has a divisive effect, and in particular, voltage-dependent inhibition produces a nonlinear current-voltage relationship.

- The suprathreshold subtractive nature of the f-I curve observed by Holt and Koch (1997) is enhanced by the voltage-dependent inhibitory conductance. Thus, voltage dependence allows for a more effective (as defined below) subtractive gain control.

- The stochastic nature of the inhibitory input leads to divisive inhibition at low firing rates, an effect enhanced by the voltage dependence of the shunting inhibition.

Section 2 presents the model of the pyramidal cell used in our study. Simulation results for the subthreshold and suprathreshold regimes follow in section 3. The simple LIF model, which clarifies the origin of the effects studied here, is examined in section 4. A conclusion and outlook are given in section 5.

2 Methods

2.1 Compartmental Model. Basilar pyramidal cells in the ELL receive segregated feedforward and feedback input (see Berman & Maler, 1999, and references therein). The former is from the electroreceptor's giving both excitatory input directly to the basal dendrite bush of the cell and disynaptic inhibitory GABAergic input to the cell soma. The feedback excitatory input is to the apical dendrites of the pyramidal cells, while the feedback inhibition is via a different set of GABAergic interneurons. Both sets of interneurons use GABA$_A$ receptors ($\tau = 7$ ms, $E_{rev} = -70$ mV).

We developed a two-dimensional, 152-compartment model of the basilar pyramidal cell using confocal images of a Lucifer yellow-filled neuron (Berman, Plant, Turner, & Maler, 1997). The diameters and length of the compartments ranged between 0.5 and 7 μm and 5 and 700 μm, respectively. However, each compartment was subdivided into a number of isopotential segments for computational purposes; the maximum section length was set to 25 μm. Here, we report only on results for inhibitory synapses ending on the soma; the use of the full model is nevertheless justified by the fact that it provides a realistic passive dendritic load on the soma compartment. The dynamical equations were integrated with NEURON (Hines & Carnevale, 1997) using a central difference scheme (Crank Nicholson). The time step was set to 0.025 ms, a value much smaller than the width of measured synaptic responses (Berman et al., 1997; Berman & Maler, 1999) and action potentials (Turner, Maler, Deerinck, Levinson, & Ellisman, 1994). For all compartments, axial resistivity was set to 250 Ω/cm, and capacitance per unit area was taken as 0.75 μF/cm^2, which are realistic values for vertebrate neurons (Mainen & Sejnowski, 1998). The passive characteristics of the model cell are such that the input resistance, $R_{in} = 30.1$ MΩ, and the passive membrane time constant, $\tau_m = 9.1$ ms, are comparable to experimental measurements (Berman & Maler, 1998a). The temperature was set at 28° C (Berman & Maler, 1998a).

2.2 Hodgkin-Huxley Dynamics. We considered the soma as having nine conductance channels. The differential equation governing the membrane potential at the soma is:

$$C_m \frac{\partial}{\partial t} V_m + I_{Na} + I_{Dr} + I_{NaP} + I_{K1} + I_{K2} + I_{KV3} + I_{leak} + I_{exc} + I_{inh} = 0. \quad (2.1)$$

The active channels involve fast sodium I_{Na} and delayed potassium I_{Dr}; they are associated with action potential generation. I_{KV3} is a high-threshold potassium channel whose kinetics are well known (Wang, Gan, Forsythe, & Kaczmarek, 1998). Kv3 is abundant in ELL pyramidal cell somata (Turner, Morales, Rashid, & Dunn, 1999; Rashid, Morales, Turner, & Dunn, 1999) and has been included for added realism. The channel parameters (see the appendix) were fitted to experimental voltage clamp tests of cloned HEK cells (Ray Turner, unpublished observations). I_{NaP} is a persistent sodium current (Mathieson & Maler, 1988; Turner et al., 1994), which is balanced by I_{K1}, a persistent potassium current. I_{K2} is a slow-activating persistent potassium current inserted to mimic the correct firing adaptation under prolonged stimulus, as observed experimentally (see the appendix). The above six channels are modeled as modified Hodgkin-Huxley channels (Hodgkin & Huxley, 1952; Koch, Bernander, & Douglas, 1995). I_{leak} corresponds to the standard leak channel. Finally, the synaptic input to the neuron is separated into an excitatory current I_{exc} and inhibitory current I_{inh}. The fitting of parameters is discussed in the appendix.

2.3 Synaptic Modeling. A synapse response is modeled as an alpha function, $g_{syn}(t) = g_{max} \frac{t}{\tau} e^{1-\frac{t}{\tau}}$ (Jack, Noble, & Tsien, 1975; Bernander et al., 1991). The function gives the synaptic conductance change for $t > t_0$, where t_0 is the synaptic response onset time. Here, g_{max} is the maximum conductance, reached at $t = \tau$, the synapse time constant. A sigmoidal form was used for the chloride channel voltage-dependent conductance (for experimental justification of sigmoidal dependence, see Figure 5c of Legendre & Korn, 1995). This synaptic conductance is still minor in comparison with the conductances underlying the action potential (g_{Na}, g_{KV3}, and g_{Dr}). We chose the following modification to the classical alpha function, in which g_{max} is made voltage dependent:

$$g_{syn}(V_m, t) = g_{max} \left(\frac{\alpha}{1 + e^{-\frac{(\lambda + V_m)}{\gamma}}} + \beta \right) \frac{t}{\tau} e^{1-\frac{t}{\tau}}. \quad (2.2)$$

Here α and β represent the degree of voltage dependence in the synapse, and λ and γ parameterize the sigmoidal dependence assumed for g_{max}. We assume that each inhibitory synapse has a fixed mean rate of firing with exponential interspike interval distribution (each is driven by a homogeneous Poisson process). Changing this mean rate varies the amount of inhibition.
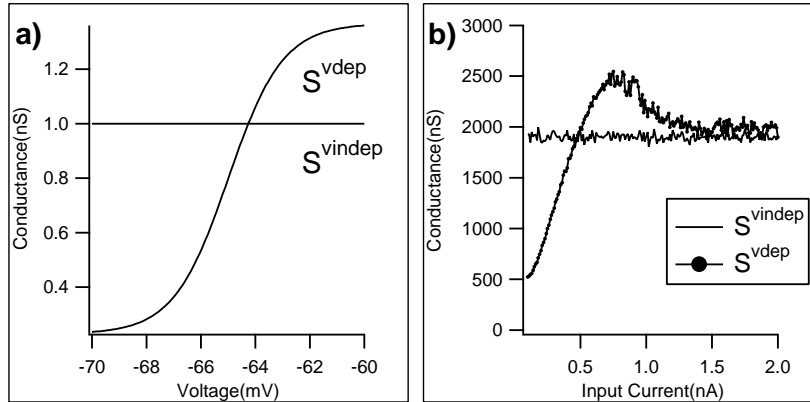
Figure 1: (a) Voltage dependence of the two conductances considered in our study. S^{vdep} refers to the voltage-dependent coefficient (large bracket in equation 2.2) with parameters $\alpha = 1$, $\beta = 0.2$, $\lambda = 65$ mV, $\gamma = 1$ mV, and multiplied by $g_{max} = 0.00114$ μS. S^{vindep} is for the voltage-independent case, with parameters $\alpha = 0$, $\beta = 1$, multiplied by $g_{max} = 0.001$ μS. These parameters are fixed throughout our study. (b) Total time-summed conductance from 250 synapses (summed conductance contributions of all synapses for the length of the simulation -1 s), each firing according to a Poisson shot-noise process with a mean rate of 10 Hz, as a function of excitatory input current. The voltage-independent curve shows no dependency on input current. The S^{vdep} curves depend on input current and in fact are similar to the average subthreshold voltage curves in Figure 2. If we let $g_{max}^{vdep} = 0.00114$ μS and $g_{max}^{vindep} = 0.001$ μS, then the integrals of both curves are approximately equal.

2.4 Quantitative Matching of S^{vindep} and S^{vdep} Synapses. Here we compare f-I characteristics for two extreme situations: the voltage-independent synapse (labeled S^{vindep}: $\alpha = 0$, $\beta = 1$) and a highly voltage-dependent synapse (labeled S^{vdep}: $\alpha = 1$, $\beta = 0.2$; note that the S^{vdep} synapse was given some voltage independence to ensure physiological realism). These parameters were adjusted so as to mimic the two- to three-fold increase in $GABA_A$ channel conductance over ~ 20 mV of membrane depolarization observed in ELL pyramidal cells in response to application of exogenous GABA (Berman & Maler, 1998a).

The λ and γ parameters were chosen to produce a gradual change in conductance over the whole subthreshold voltage range ($V_m < -60$ mV). Figure 1a shows the resulting voltage dependencies of g_{syn} that were used in the S^{vindep} and S^{vdep} simulations below. The different g_{max} values in Figure 1a were chosen based on the following considerations. In the voltage-independent case, the total synaptic conductance, summed over all synapses,

fluctuates around a constant, regardless of the excitatory input current. However, this is not so for the voltage-dependent case, where higher-input currents produce larger depolarizations, and thus larger inhibitory conductances. Figure 1b illustrates this by plotting the total time-summed conductance from 250 synapses of both types (mean rate of 10 Hz) as a function of input current. g_{max}^{vdep} in Figure 1a was chosen so that the integral of these total conductance curves (Figure 1b) is approximately equal over the 0 to 2 nA input current range. This ensures that changes in f-I characteristics due to inhibition, over the input current range of interest, are not dominated by mismatched total conductance magnitudes. For inhibitory input frequencies greater than 10 Hz, the mean subthreshold voltage will decrease, which reduces g^{vdep}. The matching is nevertheless still good.

3 Simulation Results

The total feedforward and feedback excitation I_{exc} was modeled as a constant depolarizing current I. For each such current, an average output frequency was computed over a 1000 ms window, following a 100 ms transient period. This was done for currents of 0.1 nA to 2.0 nA in increments of 0.01 nA in order to create an f-I curve for a given rate of inhibitory synaptic input. The inhibitory discharge rate was then varied in order to alter the amount of inhibition, and a new f-I curve was obtained from new simulations.

3.1 Subthreshold Dynamics: Divisive Effects and Gain Control. Figure 2 plots the average subthreshold voltage as a function of constant input current. The rheobase current I_{rh} refers to the excitatory input current required to initiate spiking for a given rate of inhibition. This current is determined by the onset of spiking in Figure 3. For $I < I_{rh}$ in Figure 2, the subthreshold voltage fluctuates around its average value, due to the stochastic nature of the inhibitory input. For $I > I_{rh}$, only the voltages in the interspike intervals (and for computational purposes, $V < -60$ mV) were used to compute the average subthreshold voltage. The shape of the maxima of these curves will be discussed later; the decrease of the average subthreshold voltage at higher input currents is the result of the increasing influence (due to the increasing spiking rate) of the repolarizing potassium currents (I_{Dr}, I_{KV3}, and I_{K1}) that follow spikes.

We ran simulations using each synapse type for 10 Hz and 15 Hz inhibitory rates. The average subthreshold voltage was computed in each case and plotted against input current. The general shape, shown in Figure 2, is similar for all plots. The S^{vindep} synapses (see Figure 2a) give a linear rise to I_{rh}, as expected from Ohm's law, and as the inhibitory strength increases from 10 Hz to 15 Hz, a divisive effect is clearly seen as a slope reduction ($\sim 25\%$). For S^{vdep} inhibition (see Figure 2b), the curve grows nonlinearly;
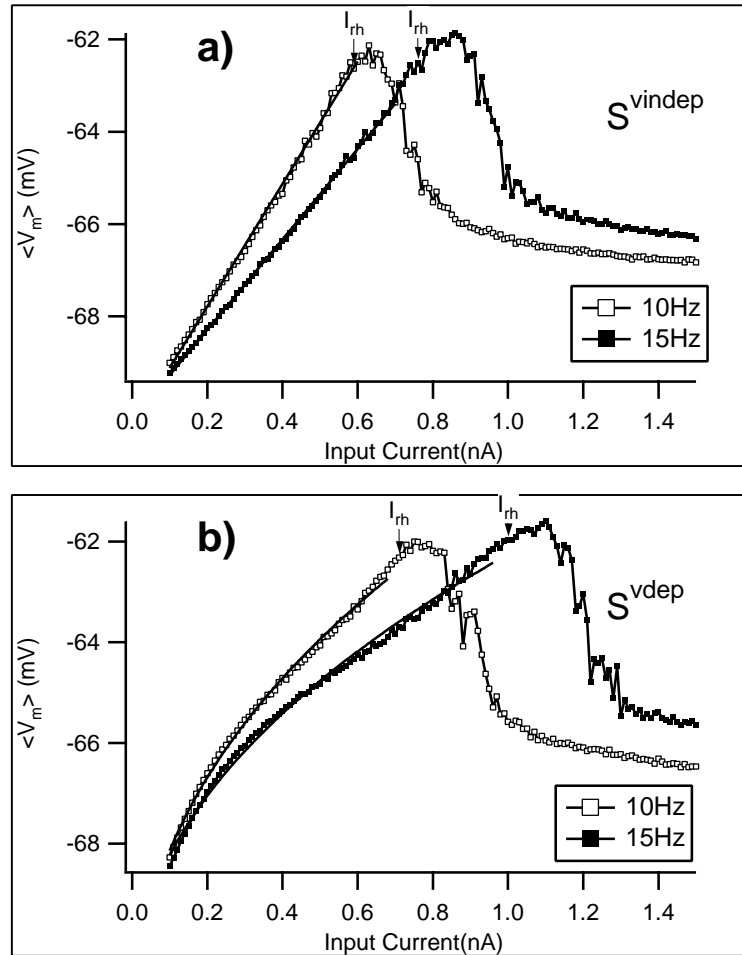
Figure 2: Average subthreshold voltage as a function of input current for (a) S^{vindep} and (b) S^{vdep} with 10 and 15 Hz inhibitory firing rates. The rheobase current I_{rh} and linear fits to the data to the left of I_{rh} are shown in *a*. I_{rh} is shifted further to the right in *b*, and the gain (slope) increases nonlinearly with input current.

a fit to ρx^{β} yielded $\beta \sim 0.44$ for the 10 Hz and $\beta \sim 0.47$ for the 15 Hz case. Again, as inhibition was increased from 10 Hz to 15 Hz, the effect on the curve is divisive, with a 20% reduction in ρ. It is seen that the linear divisive effect in Figure 2a (S^{vindep}) is constant (fixed slope) over $I < I_{rh}$. However, the divisive effect in Figure 2b (S^{vdep}) has increasing potency
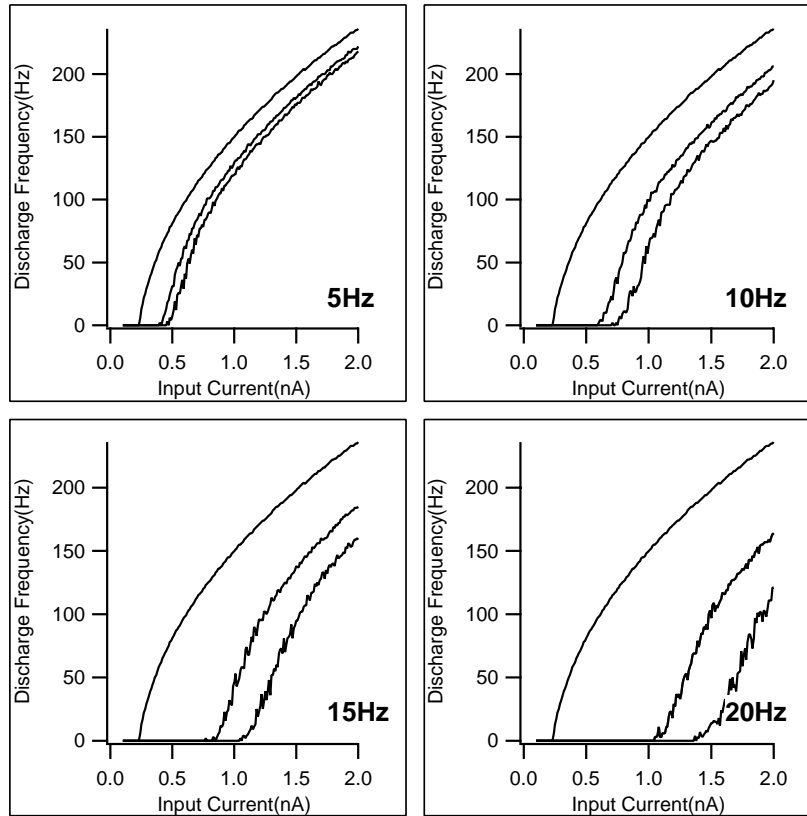
Figure 3: Mean discharge frequency versus excitatory input current for both S^{vindep} and S^{vdep} simulations. For each panel, the fixed inhibitory synaptic firing rate is indicated. In all panels the control simulation (no inhibition) is the left curve, the S^{vindep} simulation is the middle curve, and the S^{vdep} simulation is the right curve.

(slope decreases) as I approaches I_{rh}. Further, the shift in rheobase currents for both rates, $I_{rh}(15\,\text{Hz})$–$I_{rh}(10\,\text{Hz})$, is enhanced in the voltage-dependent case as a result of the nonuniform gain control. This is an explanation for the increased effectiveness of voltage-dependent inhibition near the onset of firing (see below).

3.2 Suprathreshold Dynamics: Enhanced Subtractive Inhibition for S^{vdep}**.** Figure 3 plots the mean firing rate versus input current for both synapse types and for mean inhibitory rates of 0 (control), 5, 10, 15, and 20 Hz. The observed subtractive shift (with respect to control) is seen to in-

crease with this inhibitory rate, in agreement with Holt and Koch's (1997) results obtained with a cat pyramidal cell model. Further, the subtractive shift in the S^{vdep} curves is greater than for the S^{vindep} case for equal synaptic firing rates; however, the asymptotic slope at high input current is the same in both cases. The difference in the subtractive shifts between the S^{vindep} and S^{vdep} f-I curves increases with inhibitory rate; indeed, a 0.25 nA additional current is required for the S^{vdep} simulation to reach the spiking threshold at a 20 Hz inhibitory firing rate as compared to the S^{vindep} result. Given the matching of the total time-summed conductances over the 0.1–2 nA range, discussed in section 2.4, the increased shift for voltage-dependent inhibition is not simply the result of increased amounts of inhibitory conductance. Instead, the result implies a greater effectiveness in the subtractive gain control of voltage-dependent synapses. By effectiveness, we mean that for equivalent amounts of inhibitory conductance, voltage-dependent synapses shunt a greater amount of depolarizing current than voltage-independent synapses.

This effectiveness argument is strengthened by a comparison of the f-I curves of the S^{vdep} case at 15 Hz and the S^{vindep} case at 20 Hz, shown in Figure 4a, and their associated total time-summed conductance plots given in Figure 4b (the conductance is summed over 250 synapses for the length of a simulation). Figure 4a shows f-I curves that are nearly identical for both cases, implying that the inhibitory effect is the same for both synapse types. However, Figure 4b shows that over the whole current range, the voltage-dependent total time-summed inhibitory conductance is, at all input currents, less than the voltage-independent case (this is to be expected since the S^{vdep} synapses are firing $\sim$ 25% less often than the S^{vindep} synapses). Thus, for less overall input conductance, the S^{vdep} synapses produce equivalent subtractive shifts in f-I curves. This increased effectiveness of voltage-dependent inhibition was predicted for inhibitory input to the Mauthner cell (Faber & Korn, 1987; Legendre & Korn, 1995).

The explanation of the increased effectiveness can be understood from Figure 1a, the behavior of the average subthreshold voltage (see Figure 2), and Ohm's law: $i_{inh} = g(V_m, t) \cdot (V_m - E_{rev})$. In section 2.4 we forced the time-summed conductance of both the S^{vindep} and S^{vdep} synapses to be equivalent, yet this gives no information on how the dynamics of both synapses differ. We thus give, in Figure 4c, the time series of both the somatic voltage (right axis) and the total instantaneous conductance (at each time step the conductance is summed over all synapses) of S^{vindep} and S^{vdep} (left axis) during a simulation where 250 synapses of both types fired at a mean rate of 10 Hz. The figure shows that the total instantaneous inhibitory conductance for S^{vdep} follows the somatic voltage, whereas for S^{vindep}, the conductance is approximately constant over time (fluctuations due to the stochastic nature of the inhibition). Near the spiking threshold, g^{vdep} is larger than g^{vindep}, and the opposite holds after the voltage repolarizes subsequent to a spike, as anticipated from Figure 1a. Furthermore the battery term in Ohm's law is also larger near spiking threshold than after repolarization. Since i_{inh} is the
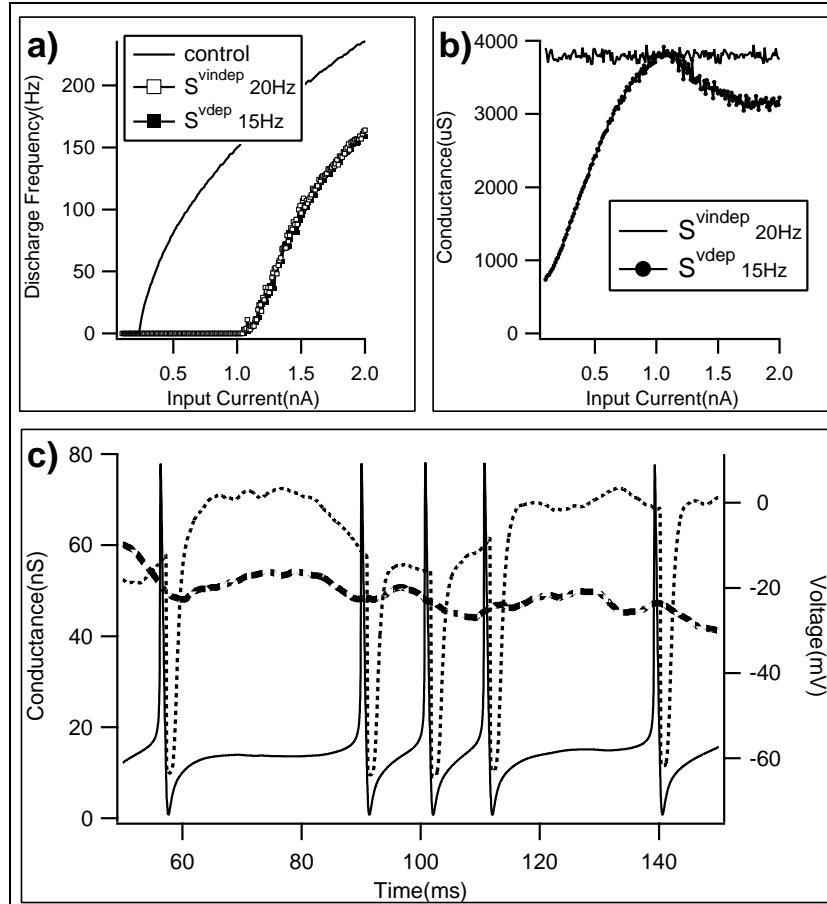
product of g^{vdep} and this battery term, then i_{inh}^{vdep} is much larger near threshold than for the voltage-independent case, where only the battery term varies with voltage. Thus, interestingly, in the voltage-dependent case, the inhibitory synapses "spread" their conductance more effectively in time, tracking the variations of the battery term. In particular, the nonuniform gain control near rheobase for g^{vdep} (see Figure 2: see section 3.1) is due to the increased conductance near threshold, which accounts for the enhanced subtractive effectiveness of voltage-dependent inhibition. We have also verified that the time-summed inhibitory currents for Figure 4c are approximately equal for both synapse types, so that the above argument applies to the inhibitory current as well for this example.

3.3 Suprathreshold Dynamics: Subtractive and Divisive Regimes. The f-I curves have an increasingly sigmoidal shape as inhibition is increased, a result of combined divisive and subtractive effects. This can be shown by separating the f-I curves into both a 0–40 Hz and a 40–100 Hz region and performing a linear regression to the data in each region to obtain f-I curve slope values. Figure 5a plots the fitted slope as a function of inhibitory rate for each region and synapse type. The region $f > 40$ Hz shows almost no change in slope for both types of inhibition: only subtractive effects are seen. Holt and Koch (1997) paid close attention to such a region where, they argued, the spike-repolarizing potassium current clamps the mean membrane potential to more negative values. The shunting inhibition then has the effect of a constant current source. Figures 2 and 5b show that the average subthreshold voltage also becomes clamped (i.e., relatively constant) at higher input currents; according to Figure 5b, this corresponds to $f > 90$ Hz. Thus, this clamping mechanism is also at work in our simulations. Interestingly, Figure 5a shows that a purely subtractive effect exists for $f > 40$ Hz, that is, before the voltage is clamped, and, further, that this effect occurs for both synapse types.

A divisive effect in the suprathreshold regime—a reduction in slope with increasing inhibition—is seen for both synapse types at lower frequencies ($f < 40$ Hz; see Figure 5a). Figure 5b shows that this divisive regime and the maximum of the voltage curve occur over the same input current range. There, the inhibitory effect is strong since the battery and conductance terms are large. Changes in excitatory input current then produce only small changes in firing frequency. Increasing the inhibitory firing rate will broaden the width of the average subthreshold voltage maximum, causing

---

Figure 4: *Facing page.* (a) Discharge frequency versus excitatory input current. The open squares are for S^{vindep} synapses with a 20 Hz firing rate, and the solid squares are for S^{vdep} synapses with a 15 Hz rate. (b) Total time-summed conductance of both synapse types as a function of excitatory input current, with the inhibitory firing rates given in *a*. Note that for all input currents, the S^{vindep} conductance is larger than the S^{vdep} conductances since the S^{vdep} synapses fire $\sim$ 25% less often. (c) Total instantaneous inhibitory conductance for both synapse types is plotted as a function of time (the heavy dashed line shows the S^{vindep} conductance, and the dotted line represents the S^{vdep} conductance, both plotted on the left axis) along with the somatic voltage caused by all ionic currents (solid line plotted on the right axis). The excitatory current was set at 1.5 nA. The simulation included 250 synapses with S^{vdep} parameters and 250 synapses with S^{vindep} parameters, both in the soma compartment. Each synaptic firing rate was set at 10 Hz. The S^{vindep} conductance fluctuates around a constant, but these fluctuations are not correlated with the voltage, as in the S^{vdep} case. Note that the data presented in *a* and *b* pertain to the same simulations, while *c* is a separate simulation, with particulars given above.
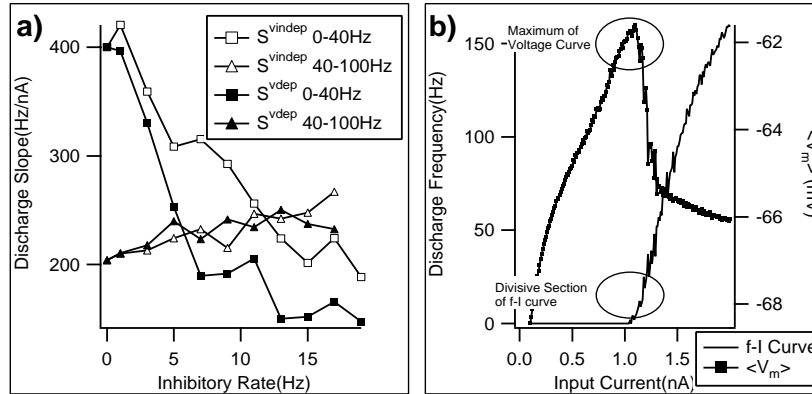
Figure 5: (a) Slope of the f-I curves (as those in Figure 3) as a function of inhibitory firing rate. The slope was determined by linear regression in two regions: 0–40 Hz and 40–100 Hz. In the 0–40 Hz region, the slope decreases with inhibition for both S^{vindep} and S^{vdep} inhibition, that is, a divisive effect is seen. In the 40–100 Hz region, no change of slope for either inhibition type is seen; this is a subtractive effect. (b) Mean discharge frequency and average subthreshold voltage as a function of input current for an S^{vdep} simulation with a mean inhibitory rate of 15 Hz at each synapse. The divisive region is marked. The region around the maximum voltage coincides with the divisive section of the f-I curve.

an initial divisive effect. This broadening of the voltage maximum is linked to the stochastic nature of the inhibition.

In the absence of inhibitory input, the average subthreshold voltage in our model displays a sharp peak at the onset of firing (not shown). This is also the case when the mean inhibition is modeled using constant (deterministic) conductances (reduction via Campbell's theorem; see Bernander et al., 1991; Holt & Koch, 1997); consequently, f-I curves then have an abrupt onset (not shown). However, a nonzero variance of the total stochastic inhibitory input causes a broadening of the maximum of the average subthreshold voltage versus input current curve (see Figure 5b); the broadening is proportional to this variance, which depends linearly on the inhibitory firing rate (by Campbell's theorem). A broad maximum is required to give the divisive regime a sufficient current interval to underlie a firing-rate region of approximately 40 Hz. This suggests that the stochastic nature of the synaptic input causes the overall sigmoidal shape of the f-I curve. We elaborate on the nature of the dependence of the divisive regime on stochastic input in the next section.

Note that the S^{vdep} simulations produce a slightly larger divisive effect since their inhibition is more effective during the voltage maximum than the

S^{vindep} cases. This is illustrated in Figure 5a in that for equivalent inhibitory rates, the estimated slope in the divisive regime is always smaller for the S^{vdep} synapse as compared to the S^{vindep} one. However, the transition from divisive to subtractive inhibition does occur for both S^{vindep} and S^{vdep}, implying that voltage dependency is not required to produce this transition (see Figures 3 and 5a).

4 Analytical Model

In this section, we further analyze our results using an LIF model. Let $g_{shunt}(V_m)$ be the conductance associated with a shunting inhibitory channel. For analytic simplicity, its voltage dependency is chosen linear in the membrane voltage V_m rather than sigmoidal:

$$g_{shunt}(V_m) = g \cdot \left(\frac{\alpha V_m}{\kappa} + \beta \right). \tag{4.1}$$

Here g is the overall strength of the inhibition, α and β are dimensionless parameters that control the degree of voltage dependency (similar to α and β in equation 2.2), and κ is introduced to preserve dimensionality and force both linear and constant terms to be similar in magnitude (we choose $\kappa = 5$ mV, the midpoint between reset and threshold voltage). Assuming only this shunting inhibition and a constant excitation, we have

$$C_m \frac{dV_m}{dt} + g \cdot \left(\frac{\alpha V_m^2}{\kappa} + \beta V_m \right) = 1. \tag{4.2}$$

The subthreshold case yields the steady-state voltage V_{ss}:

$$V_{ss} = \frac{-\beta\kappa}{2\alpha} + \frac{1}{2}\sqrt{\frac{\beta^2\kappa^2}{\alpha^2} + \frac{4\kappa I}{g\alpha}} \ . \tag{4.3}$$

For $\beta \gg \alpha$ (voltage-independent inhibition), V_{ss} is linear in I, while for $\beta \ll \alpha$ (voltage-dependent inhibition), V_{ss} rises nonlinearly, as is the case in Figure 2b for the full ionic model. The case where the steady-state voltage equals the threshold voltage, $V_{ss} = V_{thres}$, corresponds to $I = I_{rh}$. Inserting these relations into equation 4.3 yields

$$I_{rh} = \frac{\alpha g V_{thres}^2}{\kappa} + g\beta V_{thres}. \tag{4.4}$$

Equation 4.4 thus shows that as the inhibition becomes increasingly voltage dependent (i.e., as α/β increases), the rheobase current I_{rh} shifts to higher values. This shift is also seen in the compartmental simulations (see Figure 3).
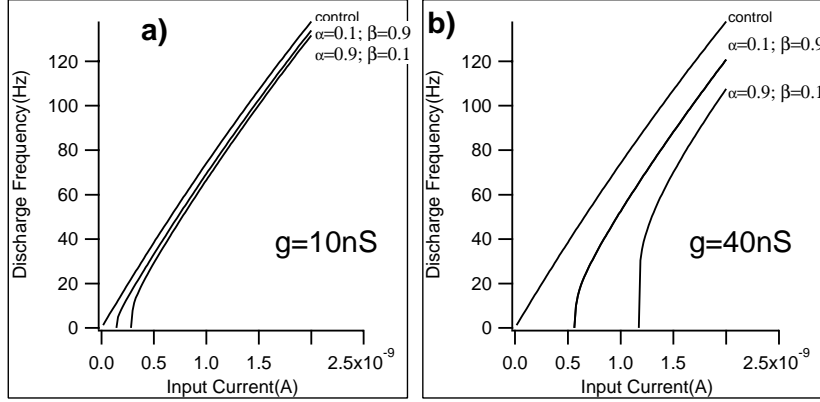
Figure 6: Mean firing frequency versus input current in the LIF model. (a) Constant g of 10 nS (weak inhibition). (b) Constant g of 40 nS (strong inhibition). In each graph, the control case for $g = 0$ is shown. Each graph displays results for weak voltage dependence ($\alpha < \beta$) and strong voltage dependence ($\alpha > \beta$). Other parameter values are $C_m = 1$ nF, $k = 5$ mV, $V_{th} = 10$ mV, $t_0 = 0.001$ s.

Further, equation 4.2 is an analytically tractable Ricatti equation (Davis, 1962), with solution for $V_m(0) = 0$:

$$V_m(t) = \frac{\eta}{2g\alpha} \tanh\left(\frac{\eta t}{2\kappa C_m} + \arctan h\left(\frac{\eta \beta}{\kappa \beta^2 g + 4\alpha I}\right)\right) - \frac{\beta \kappa}{2\alpha}, \qquad (4.5)$$

where $\eta = \sqrt{(\kappa g \beta)^2 + 4\alpha g I \kappa}$. We can derive frequency of discharge f from equation 4.5. Letting $V_m(T) = V_{thres}$ yields the period T between spikes:

$$T = \frac{2\kappa C_m}{\eta} \cdot \left(\arctan h\left(\frac{2g\alpha V_{th} + g\kappa}{\eta}\right) - \arctan h\left(\frac{\eta \beta}{\kappa \beta^2 g + 4\alpha I}\right)\right). \qquad (4.6)$$

The frequency of discharge is then $f = 1/(T + t_o)$, where we have added an absolute refractory period t_0 ($\sim$ 1 ms). Figure 6 plots this frequency versus input current for two extreme cases: high β and low α (weakly voltage dependent) and low β and high α (strongly voltage dependent). We chose to keep $\alpha + \beta = 1$ in all plots so as to ensure that the inhibitory strength is controlled by g only, and not by α and β. Increasing g corresponds to increasing the inhibitory firing rate in the compartmental model. According to Campbell's theorem, these two quantities are linearly related. The subtractive effect and its increase with g, found in the compartmental model, is clearly reproduced by this LIF model, as seen in Figure 6. The increased subtractive effectiveness for the voltage-dependent case (for fixed g) is also seen.

Note that in our LIF model, we have used a linear approximation to the sigmoidal dependence used in the compartmental model. Nevertheless, qualitatively similar results are obtained in both cases. This indicates that the exact dependence of $g(V_m)$ on V_m is not important to establish increased effectiveness of voltage-dependent conductance; only a monotonic increasing function is required. As verification, we have also incorporated a sigmoidal dependence in our LIF model and obtained f-I curves using numerical integration (fourth-order Runge-Kutta, fixed time step of 10^{-5}). The results (not shown) are qualitatively similar. This not only illustrates the robustness of the model mentioned above, but also provides further evidence that the increased subtractive effectiveness of voltage-dependent inhibition is a consequence of the voltage dependence rather than of some unsuspected dynamical effect in the full ionic model.

Finally, we recall that the divisive effect ($f < 40$ Hz) seen in the compartmental model was a consequence of the stochastic nature of the inhibition. Our LIF model does not have a stochastic input, and its average subthreshold voltage curve has a sharp peak at the onset of periodic firing (not shown). This deterministic model produces purely subtractive f-I curve shifts through inhibition (see Figure 6). However, the inclusion of stochastic input in the LIF model is known to produce sigmoidal f-I curves as in Figure 3 (see, e.g., Lánský & Sato, 1999, and Figure 7 in this article). Stochastic forcing also broadens the peak of the average subthreshold voltage versus input current curves as in Figure 5b (not shown). In view of this, we have set out to determine (1) whether a subtractive effect is also present with stochastic synaptic input and (2) whether stochastic input produces a divisive regime at lower firing frequencies, as in the compartmental model.

For simplicity we considered only the voltage-independent case ($\alpha = 0$) of equation 4.1, since divisiveness was also seen for the S^{vindep} synapses in the compartmental simulations (see Figure 5a). There are a variety of ways in which a stochastic synaptic model with reversal potentials can be approximated by diffusion models (Lánský & Sato, 1999). Here we let the conductance g in the LIF model be a stochastic quantity by setting $g = \bar{g} + \sigma(g)\eta(t)$ where $\bar{g}$ is the mean conductance and $\eta(t)$ is a stochastic process of standard deviation $\sigma(\bar{g})$. To match the smoothness of the conductance fluctuations in the compartmental model, we model $\eta(t)$ as an Ornstein-Uhlenbeck process (lowpass-filtered gaussian white noise) with correlation time $\tau = 75$ ms; our results were not qualitatively sensitive to this correlation time. Equation 4.1 thus becomes a stochastic differential equation with multiplicative noise (since the noise term multiplies the state variable V_m):

$$C_m \frac{\partial V_m}{\partial t} + \left[\bar{g} + \sigma(\bar{g})\eta(t)\right] V_m = I \qquad (4.7')$$

$$\frac{\partial \eta}{\partial t} = -\frac{\eta}{\tau} + \xi \qquad (4.7'')$$

where ξ is gaussian white noise with zero-mean and unit standard deviation. Numerical simulations produced sigmoidal curves of mean firing rate versus input current I (see Figure 7), as expected. Increases in inhibitory firing rate in the compartmental model were modeled here as increases in mean conductance $\bar{g}$; these increases are linearly related, as discussed above. Further, and also in accordance with Campbell's theorem, the variance σ^2 of the conductance fluctuations was increased linearly with the inhibitory firing rate, and thus with $\bar{g}$. Figure 7a shows that the inclusion of this stochastic forcing produces f-I curve shifts that are qualitatively similar to those found for the deterministic LIF and compartmental models; hence, subtractive inhibition (Holt & Koch, 1997) is maintained in the presence of such forcing.

Figure 7a also clearly shows a divisive effect as $\bar{g}$ increases, as in the compartmental model. The origin of this effect here may lie in the coupling of the variance of the fluctuations to their mean or in the multiplicative nature of the noise, or in both. Figure 7b presents f-I curves from simulations in which the variance was made independent of $\bar{g}$. Although the noise is still multiplicative, divisiveness is no longer seen. We have also verified that a stochastic LIF with additive noise (i.e., stochastic forcing is simply added to the right-hand side of equation 4.1) shows divisiveness as well, as long as the variance increases with the mean conductance (not shown). Thus, the divisiveness seen in the LIF model, and presumably in the compartmental model as well, arises from increases in the variance of the stochastic forcing that accompanies increases in inhibitory input.

The origin of the effect can be seen by comparing the right-most curves in Figures 7a and 7b. The point of firing onset is one of the two points used for estimating the slope of the f-I curve at lower discharge frequencies. The second point is determined by the intersection of the stochastic f-I curve with a line of constant firing frequency (e.g., 40 Hz was used in the compartmental model; 10 Hz could be used for the LIF model in Figure 7). The onset of firing in Figure 7a occurs at a lower input current than in Figure 7b; this is a consequence of the higher conductance variance in Figure 7a. Since the estimated slope is inversely proportional to the input current interval between these two points, it is smaller in Figure 7a than in Figure 7b.

Further, in the voltage-dependent conductance case, the effectiveness of the inhibition is increased, particularly near the onset of firing (see Figure 1b). This increases the input current interval used for the slope estimation, yielding a smaller slope in comparison with the voltage-independent case. Thus, voltage dependence further enhances divisiveness.

5 Conclusion and Outlook

We have presented a morphologically and physiologically realistic compartmental model of a pyramidal cell in the electrosensory lateral line lobe of a weakly electric fish. This model was then used to investigate the effect of voltage-dependent inhibitory conductances on firing rate versus input
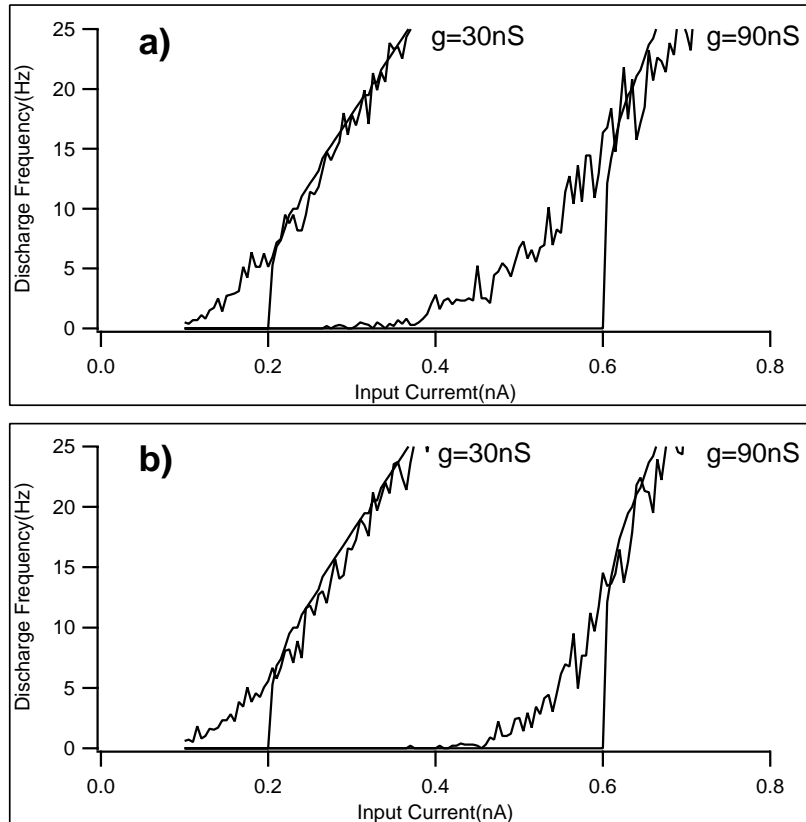
Figure 7: Mean firing rate f versus input current I for the stochastic LIF model, given by equations 4.7 and 4.7'. Firing rates were calculated at 0.01 nA steps using 10 sec simulations for each input current. (a) The mean inhibitory conductance (voltage independent) is proportional to the firing rate of Poisson inputs, while the standard deviation is proportional to the square root of this firing rate (Campbell's theorem). Here we choose $\sigma = a\sqrt{\bar{g}}$ with $a = 3 \times 10^{-4}$. A clear divisive effect at low firing frequencies ($f < 10$ Hz) is present as $\bar{g}$ increases from 30 nS to 90 nS. (b) The standard deviation of the conductance is now made constant at $\sigma = b$, with $b = 5 \times 10^{-8}$. No divisiveness is present as $\bar{g}$ increases. In all plots, the deterministic curve ($\sigma = 0$) is superimposed. The stochastic integration used a fixed step (10^{-5} sec) fourth-order Runge-Kutta method combined with the Box-Muller algorithm for the gaussian deviates.

current curves. To our knowledge, this article is the first to model this dependence explicitly, and it highlights the importance of this dependence, especially when dealing with the subthreshold regime. Our results show

that this kind of shunting inhibition enhances the subtractive shifts reported in Holt and Koch (1997) and indicates an increased effectiveness of voltage-dependent inhibitory conductances compared to the commonly assumed voltage- independent ones. This is due to the tracking of the membrane potential by the inhibitory conductance, such that the inhibitory effect is maximal near the onset of spiking. One interesting implication of this increased effectiveness is that small changes in inhibitory conductance, arising, for example, from synaptic plasticity, can have strong effects on gain control in sensory systems (Nelson, 1994; Nelson & Paulin, 1995).

We have also uncovered a divisive regime at low firing frequencies. It relates to the broadening of the peak of the average subthreshold voltage versus input current characteristic, a consequence of the stochastic nature of the inhibitory synaptic input. Our study of the LIF model reveals that the conductance fluctuations used to model the randomness of the Poisson inputs in the compartmental model are responsible for producing a divisive regime at lower discharge frequencies; this is true provided that the variance of these fluctuations increases with the mean conductance. This divisiveness is enhanced by the voltage dependence of the conductance. However, these fluctuations do not alter the subtractive nature of the f-I curves at higher discharge frequencies or their enhancement by voltage-dependent conductances.

The spontaneous firing rate of some classes of ELL pyramidal cells is well below 40 Hz (Bastian & Courtwright, 1991). During electrolocation of prey objects (Nelson & MacIver, 1999), only small alterations of electroreceptor input occur, and it is therefore likely that firing-rate modulations of these pyramidal cells will remain in the divisive regime. Therefore, divisive inhibition of ELL pyramidal cells is functionally relevant for electroreception and likely relevant for other neural networks as well.

Future work should analyze further the possible interactions of voltage-dependent inhibition with various voltage-gated inward currents present in ELL pyramidal cells (NMDA: Berman et al., 1997; persistent sodium channels: Stuart, 1999; Turner et al., 1994; potassium conductances: Berman & Maler, 1998b) Further, our study has been performed for fixed inhibitory rates. However, the inhibitory firing rates are likely to be correlated with ELL pyramidal cell firing rates (Berman & Maler, 1999). It will be interesting to investigate the effect of voltage-dependent inhibition in closed loop (Nelson, 1994; Nelson & Paulin, 1995). Finally, it will be important to incorporate eventually more realistic excitatory synaptic input with variable degrees of correlation with inhibitory input (Berman & Maler, 1999).

Appendix ‾‾‾‾‾‾‾‾‾‾‾‾‾‾‾‾‾‾‾‾‾‾‾‾‾‾‾‾‾‾‾

In this appendix, we provide details on the estimation of parameters for the pyramidal cell ionic model. The qualitative conclusions of our article do not depend sensitively on the exact values of our parameters. Figure 8
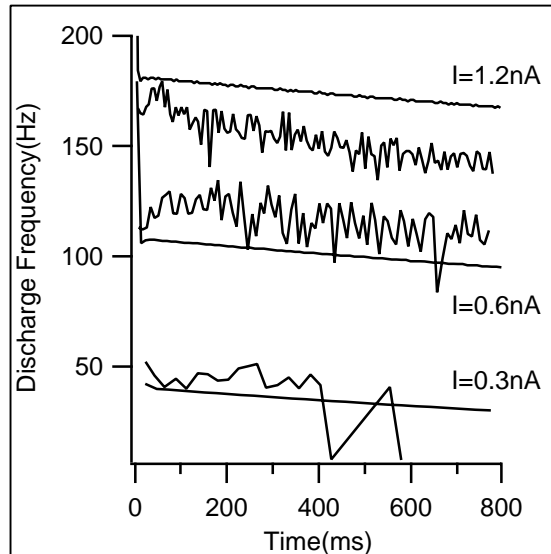
Figure 8: Mean discharge frequency versus time from our simulations and from a single cell in vitro recording (Berman & Maler, 1998b). Parameters are as in Table 1. The bottom two traces give the experimental and simulation results for a current injection of 0.3 nA, the middle two for a current of 0.6 nA, and the top two for a current of 1.2 nA. The simulations were compared to all currents from 0.1 to 1.2 nA in steps of 0.1 nA (the other nine plots are not shown).

plots firing frequency versus time for both a real ELL basilar pyramidal cell under constant depolarization (0.3 nA, 0.6 nA, and 1.2 nA injections), as well as the compartmental model measurements under equivalent conditions. We adjusted active and leak channel parameters to obtain reasonable agreement between simulated and measured firing frequency versus time plots for a range of excitatory input currents (Mathieson & Maler, 1988). The final parameters are shown in Table 1. Good agreement is found for 0.3 and 0.6 nA, with increasing discrepancies as the current increases. The inclusion of a fourth potassium conductance, which will mimic the proper firing saturation at high currents, is planned. The growth of the model is an ongoing process, yet this parameter choice is deemed reasonable, given the variability observed in such experimental data, and the issues addressed here.

Acknowledgments

Table 1: Ionic Channel Parameters.

	I_{Na}	I_{Dr}	I_{NaP}	I_{K1}	I_{K2}	I_{KV3}	I_{leak}
Ion	Na^+	K^+	Na^+	K^+	K^+	K^+	N/A
η	m^2h	m^2	m^3	m	m	m^3h	N/A
a/b	$40/-3$	$40/-3$	$50/-7$	$42/-5$	$30/-1$	$0/-18$	N/A
	$45/3$					$0/40$	
τ (ms)	0.2	0.4	0.1	2.0	4000	2.0	N/A
	0.6					2.0	
E_{rev} (mV)	$+50$	-95	$+50$	-95	-95	-95	-70
g_{max} (S/cm^2)	0.85	0.5	0.03	0.01	0.015	5	7E-5

Notes: Each current is described by $I = g_{max}\eta$. E_{rev} is the reversal potential of the channel. g_{max} is the maximum conductance of the channel. $\eta = m^i h^j$ is the product of the activation and inactivation variables raised to powers i and j, respectively. τ is the voltage-independent time constant associated with m or h. a and b are the constants appearing in the sigmoid expression for m_∞ and h_∞: $x_\infty = 1/1 + \exp((V_m + a)/b)$. The state variable x evolves as $\frac{\partial x}{\partial t} = \frac{x_\infty - x}{\tau_x}$. The columns for I_{Na} and I_{KV3} contain double entries in some blocks; the top entry is associated with the m parameter, the bottom with the h.

References

Abbott, L. F. (1991). Realistic synaptic inputs for model neural networks. *Network, 2*, 245–258.

Abbott, L. F., Varela, J. A., Sen, K., & Nelson, S. B. (1997). Synaptic depression and cortical gain control. *Science, 275*, 220–223.

Bastian, J., & Courtwright, J. (1991). Morphological correlates of pyramidal cell adaptation rate in the electrosensory lateral line line lobe of weakly electric fish. *J. Comp. Physiol A., 168*, 393–407.

Berman, N., & Maler, L. (1998a). Inhibition evoked from primary afferents in the electrosensory lateral line lobe of the weakly electric fish. *J. Neurophysiol., 80*, 3173–3196.

Berman, N., & Maler, L. (1998b). Interaction of GABA$_B$-mediated direct feedback inhibition with voltage-gated currents of pyramidal cells in the electrosensory lateral line lobe. *J. Neurophysiol., 80*, 3197–3213.

Berman, N., & Maler, L. (1998c). Distal vs proximal inhibitory shaping of feedback excitation in the lateral line lobe. *J. Neurophysiol., 80*, 3214–3232.

Berman, N., & Maler, L. (1999). Neural architecture of the electrosensory lateral line lobe: Adaptations for coincidence detection, a sensory searchlight and frequency-dependent adaptive filtering. *J. Exp. Biol., 202*, 1243–1253.

Berman, N., Plant, J., Turner, R., & Maler, L. (1997). Excitatory amino acid receptors at a feedback pathway in the electrosensory system: Implications for the searchlight hypothesis. *J. Neurophysiol., 78*, 1869–1881.

Bernander, O., Douglas, R., Martin, K., & Koch, C. (1991). Synaptic background activity influences spatiotemporal integration in single pyramidal cells. *Proc. Natl. Acad. Sci. USA, 88*, 11569–11573.

Carandini, M., & Heeger, D. (1994). Summation and division by neurons in primate visual cortex. *Science, 264*, 1333–1336.

Davis, H. (1962). *Introduction to nonlinear differential and integral equations*. New York: Dover.

Faber, D., & Korn, H. (1987). Voltage-dependence of glycine-activated Cl-channels: A potentiometer for inhibition? *J. Neuroscience, 7*, 807–811.

Hines, M. L., & Carnevale, N. T. (1997). The neuron simulation environment. *Neural Comp., 9*, 1179–1209.

Hodgkin, A., & Huxley, A. (1952). A quantitative description of membrane current and its application to conduction and excitation in nerve. *J. Physiol., 117*, 500–544.

Holt, G., & Koch, C. (1997). Shunting inhibition does not have a divisive effect on firing rates. *Neural Comp., 9*, 1001–1013.

Jack, J., Noble, D., & Tsien, R. (1975). *Electric current flow in excitable cells*. New York: Oxford University Press.

Koch, C., Bernander, O., & Douglas, R. (1995). Do neurons have a voltage or a current threshold for action potential initiation? *J. Comp. Neuroscience, 2*, 63–82.

Koch, C., & Poggio, T. (1992). Multiplying with synapses and neurons. In T. McKenna, J. Davis, & S. Zornetzer (Eds.), *Single neuron computation*. Orlando, FL: Academic Press.

Lánský, P., & Sato, S. (1999). The stochastic diffusion models of nerve membrane depolarizations and interspike interval generation. *J. Peripheral Nervous System, 4*, 27–42.

Legendre, P., & Korn, H. (1995). Voltage dependence of conductance changes evoked by glycine release in the zebrafish brain. *J. Neurophysiol., 73*, 2404–2412.

Mainen, Z. F., & Sejnowski, T. J. (1998). Modeling active dendritic processes in pyramidal neurons. In C. Koch & I. Segev (Eds.), *Methods in neuronal modeling: From ions to networks*. Cambridge, MA: MIT Press.

Mathieson, W. B., & Maler, M. (1988). Morphological and electrophysiological properties of a novel *in vitro* preparation: The electrosensory lateral line lobe brain slice. *J. Comp. Physiol. A, 163*, 489–506.

Nelson, M. E. (1994). A mechanism for neuronal gain control by descending pathways. *Neural Comp., 6*, 255–269.

Nelson, M. E., & MacIver, M. (1999). Prey capture in the weakly electric fish *Apteronotus albifrons*: Sensory acquisition strategies and electrosensory consequences. *J. Exp. Biol., 202*, 1195–1203.

Nelson, M. E., & Paulin, M. G. (1995). Neural simulations of adaptive reafference suppression in the elasmobranch electrosensory system. *J. Comp. Physiol. A, 177*, 723–736.

Rashid, A., Morales, E., Turner, R. W., & Dunn, R. J. (1999). Molecular characterization of two Kv3-type K channels in a vertebrate sensory neuron. *XXIX Proc. Soc. Neurosci., 25*, 2248.

Rose, D. (1977). On the arithmetical operation preformed by inhibitory synapses onto the neuronal soma. *Exp. Brain. Res., 28*, 221–223.

Segal, M., & Barker, J. (1984). Rat hippocampal neurons in culture: Properties of GABA activated Cl$^-$ ion conductance. *J. Neurophysiol., 51*, 500–515.

Stuart, G. (1999). Voltage-activated sodium channels amplify inhibition in neocortical pyramidal neurons. *Nature Neuroscience, 2*, 144–150.

Tsodyks, M. V., & Markram, H. (1997). The neural code between neocortical pyramidal neurons depends on neurotransmitter release probability. *Proc. Nat. Acad. Sci., 94*, 719–723.

Turner, R. W., Maler, L., Deerinck, T., Levinson, S., & Ellisman, M. (1994). TTX-sensitive dendritic sodium channels underlie oscillatory discharge in a vertebrate sensory neuron. *J. Neurosci., 14*, 6453–6471.

Turner, R. W., Morales, E., Rashid, A., & Dunn, R. J. (1999). Characterization of an Apteronotid Kv3 potassium channel. *XXIX Proc. Soc. Neurosci., 25*, 193.

Yoon, K. W. (1994). Voltage-dependent modulation of GABA$_A$ receptor channel desensitization in rat hippocampal neurons. *J. Neurophysiol., 71*, 2151–2160.

Wang, L. Y., Gan, L., Forsythe, I. D., & Kaczmarek, L. K. (1998). Contribution of the Kv3.1 potassium channel to high-frequency firing in mouse auditory neurons. *J. Physiol. Lond., 509*, 183–194.